Comparison of Shack-Hartmann and digital holographic wavefront sensing using a benchtop turbulence generator

Timothy J. Bukowski*[a,b], Matthew Kalensky[a], Darren Getts[a], and Stanislav Gordeyev[b]

[a]Integrated Engagement Systems Department, Naval Surface Warfare Center Dahlgren Division, Dahlgren, Virginia, 22448
[b]University of Notre Dame, Notre Dame, Indiana, 46556

ABSTRACT

This work presents a comprehensive characterization of a benchtop optical-turbulence simulator system using a Shack—Hartmann (SH) wavefront sensor, an off-axis digital holography (DH) wavefront sensor, and a far-field imaging camera. The system employs two spatial-light modulators (SLMs) to impose turbulent phase screens with prescribed statistics onto a laser beam, simulating atmospheric turbulence. We conduct tests to compare the system's performance against wave-optics simulations by varying turbulence strength, varying the modeled propagation distance, and using both SLMs to model beam propagation. The results show that the DH wavefront measurements have a root mean square error (RMSE) of 0.02–0.03 µm compared to the simulated wavefronts, while the SH measurements have a RMSE of 0.02–0.05 µm compared to the DH wavefront measurements. We also assess the system's ability to model beam propagation. Here, we find that the extent of phase disagreement increases with increasing propagation distances. Overall, the results of a Monte–Carlo simulation that models a 25 cm beam along a 1 km path reveal that DH measurements closely match the known turbulence parameters whereas the SH measurements generally underestimate turbulence strength. At large, this work informs system designers of how different wavefront sensors perform in varying optical-turbulence conditions.

Keywords: digital holography, Shack–Hartmann wavefront sensor, atmospheric optical turbulence, adaptive optics, scintillation, spatial light modulator

1. INTRODUCTION

Atmospheric turbulence leads to a degradation in laser propagation system performance. In practice, we employ adaptive-optics (AO) systems to compensate for the deleterious effects of atmospheric turbulence on these systems. Here, AO systems use a wavefront sensor to measure the aberrations on the beam, and we compensate for the aberrations using a deformable mirror. For a beam propagating through strong distributed-volume turbulence, phase aberrations give rise to constructive and destructive interference which results in irradiance fluctuations known as scintillation.[1] Locations with total destructive interference will give rise to branch points where the irradiance goes to zero and the phase is undefined. Branch points have a helical phase and form in pairs of opposite charge. The combined effects of strong scintillation and branch-point formation lead to practical challenges for system designers. For example, consider the Shack–Hartmann wavefront sensor (SHWFS). This sensor has been used to measure wavefront aberrations in AO systems for decades. In practice, we use a SHWFS to estimate wavefront gradients which we then use in a least-squares reconstruction algorithm to obtain a continuous estimate of the wavefront. Researchers have shown that scintillation degrades the accuracy of the SHWFS measurement.[2] When appreciable scintillation is present, we can have (1) signal dropouts, (2) wavefront-gradient measurement errors (C-tilt $\neq$ G-tilt[2,3]), and (3) branch-point formation. Regarding branch-point formation, any branch points in the phase get mapped to the null space of the reconstruction algorithm, and their associated phase is known as the hidden phase.[1,4,5] Researchers have explored methods for identifying branch points from SHWFS data; however, it remains an open research question as to whether this information can be used to generate a sufficient hidden-phase estimate.[1,5–12] Under traditional operation, the inability of

*Further author information:
E-mail: tbukowski@nd.edu, Telephone: (574) 631-4280

Unconventional Imaging, Sensing, and Adaptive Optics 2024, edited by Jean J. Dolne, Santasri R. Bose-Pillai, Matthew Kalensky, Proc. of SPIE Vol. 13149, 1314910
© 2024 SPIE · 0277-786X · doi: 10.1117/12.3026892

the SHWFS combined with a least-squares reconstructor to provide hidden phase leads to a decrease in AO system performance. For these reasons, researchers have explored the efficacy of other wavefront sensors in strong scintillation environments. Digital holography (DH), for example, is an interferometric wavefront sensor which has been shown to be resilient to scintillation and branch points.[13–16] Digital holography allows you to measure the complex-optical field with great spatial resolution.[17]

It is clear that there is a considerable amount of research to be conducted regarding the benefits and drawbacks of different wavefront sensors operating in adverse optical-turbulence conditions. However, one challenge associated with these research topics is contending with the ever-changing nature of the atmosphere. Therefore, it is desirable to be able to create a repeatable atmospheric environment in a laboratory setting in order to study atmospheric effects on optical systems in a controlled manner. There many ways to go about this from using transmissive phase screens,[18] to spinning etched phase wheels,[19] to heating the air with a hot plate.[20] For the work conducted here, we employ spatial-light modulators (SLMs). SLMs use liquid-crystal displays to impose a user-defined phase pattern onto the beam. In this work, we impose atmospheric turbulence phase screens onto the SLMs and propagate a beam through our system using a combination of 4f relays and optical trombones. At the output of the system, we are able to measure the phase aberrations imposed onto the beam using both a SH and DH wavefront sensor. A similar system was designed and used in Ref. 21.

In this paper, we characterize the performance of our benchtop turbulence-generator system using SH and DH wavefront sensor measurements. We then compare the results of these tests to simulation results. Section 2 reviews the wavefront sensors used in this system. Section 3 describes the turbulence generator system and the wave-optics simulation that it was designed to resemble. Section 4 qualitatively compares the sensor measurements with simulation, then quantitatively compares turbulence statistics between experiment and simulation. Section 5 summarizes the results.

2. WAVEFRONT SENSING

2.1 Shack–Hartmann Wavefront Sensor

A SHWFS is comprised of an array of subaperture lenslets which focus incident light onto a camera detector. Here, the average gradient of the incoming phase aberration over each subaperture in the lenslet pupil is estimated from irradiance-pattern deflections in the image plane.[22,23] Subsequently, these so-called slope estimates are traditionally used in a least-squares reconstructor to estimate the continuous Optical-Path Difference (OPD) aberration. The wavefront can then be found as $WF = -OPD$.

For the work presented here, a baseline SHWFS image was collected without turbulence applied to the SLMs in order to capture any aberrations associated with the system's optical components. We also used this baseline SHWFS image as the reference from which we calculate turbulence-induced displacements.

2.2 Digital Holography Wavefront Sensor

Digital holography is an interferometric technique that measures the complex-optical field of the beam. Our setup uses an off-axis pupil plane recording geometry where the signal beam is interfered with a tilted planar reference beam onto a camera sensor, creating a fringe pattern or hologram. An example hologram is shown in the top left plot of Fig. 1. We also present a zoomed-in view in the bottom left of the image to better show the fringe pattern. This hologram is 2D fast Fourier transformed and then filtered to isolate the signal-reference crossterm. This crossterm is depicted with the red circle in the top-right plot of Fig. 1. Subsequently, the term is shifted to the origin, then inverse Fourier transformed to give the complex-optical field. This process is described in further detail in Refs. [15, 17, 24, 25]. The size of the filtered window was chosen to be about twice the diameter of the crossterm of the strongest turbulence case. This allows translation of the peak resulting from tip/tilt aberration on the beam. A 2×2 pixel average filter was applied to the complex-optical field to reduce noise. Similar to the SHWFS case, a baseline image was taken without turbulence applied to the SLMs in order to measure aberrations inherent to the optics setup. This baseline complex-optical field was then removed as $\Psi = \Psi_{measured}/\Psi_{baseline}$ from future measurements to isolate the turbulence-induced effects. This baseline image removal also removes the conjugate reference complex-optical field that is superimposed in the output complex-optical field in digital holography. After applying these post-processing steps, the desired phase of the complex-optical field was then

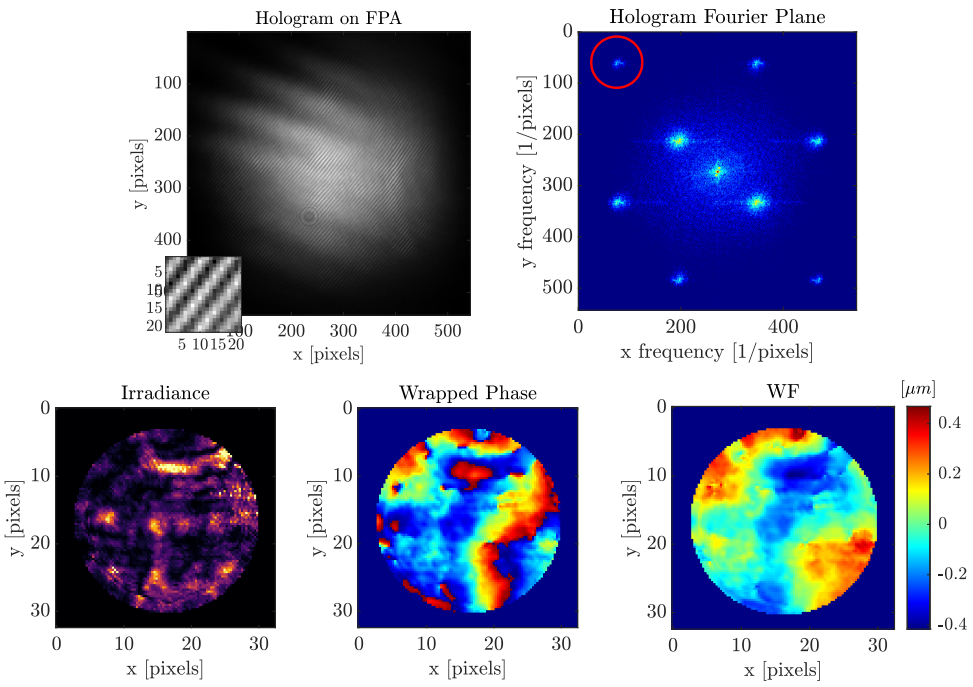


Figure 1. Processing steps of digital holography. Top left shows the hologram measured on camera. Top right shows the magnitude of the 2D Fourier transform of the hologram, with the filtered out signal shown in red. The bottom row shows the irradiance, phase, and unwrapped wavefront of the beam.

unwrapped using a least-squares unwrapping algorithm and converted to a wavefront as $WF = \frac{\phi\lambda}{2\pi}$, where ϕ is the phase and λ is the wavelength. An example frame where we imposed turbulence onto the beam is shown in Fig. 1 where we plot the measured irradiance in the bottom-left plot, wrapped phase in the bottom-middle plot, and unwrapped phase in the bottom-right plot. Note that the Fourier plane has many peaks, when we only expect to see three (the autocorrelation peak with the two conjugate cross-terms). The other spurious peaks are due to diffraction from the SLM. When we isolated the desired cross-term, we made sure to avoid contamination from the other peaks present in the Fourier plane.

3. SIMULATION AND EXPERIMENTAL SETUP

3.1 Wave-Optics Simulations

Wave-optics simulations were conducted to compare the simulated phase and irradiance with the phase and irradiance measured at the output of the turbulence generator using the SHWFS and DHWFS. In these simulations, a collimated beam was transmitted through phase screens via angular-spectrum propagation. The phase screens were generated by filtering Gaussian white noise[26–28] and spherical-wave angular-spectrum propagation was accomplished using the split-step beam propagation method.[26–31] After propagation, the complex-optical field was received using an aperture transmittance function. For these simulations, phase screens were created for a range of C_n^2 values. For each simulation, the phase from the received complex-optical fields was used in a least-squares unwrapping algorithm. Subsequently, the phase was then converted to wavefronts by scaling by laser wavenumber. A Gaussian beam with a wavelength of $\lambda = 633$ nm and a width of 0.25 m was used for all simulations.

3.2 SLM Turbulence Generator

Benchtop turbulence-generator systems help bridge the gap between wave-optics simulations and real atmospheric propagation by allowing for beam propagation and adaptive-optics tests in an environment with repeatable

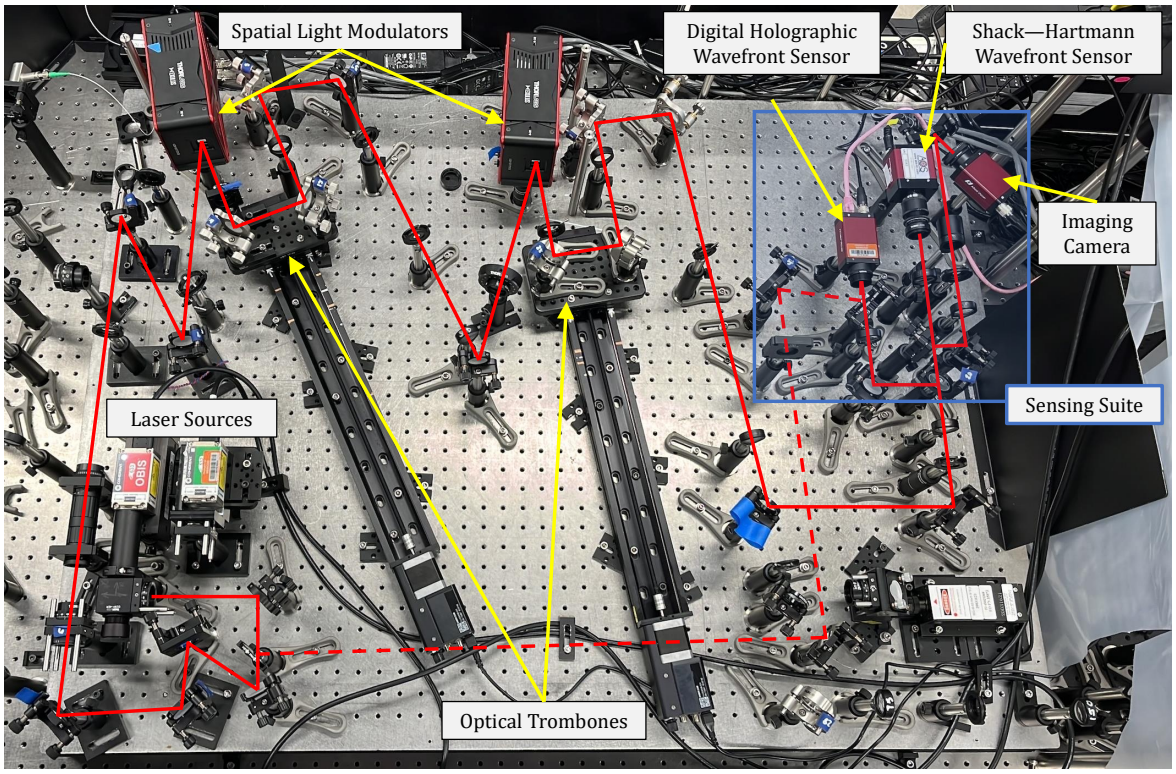


Figure 2. SLM-based turbulence generator setup. The solid-red line shows the signal beam path, while the dashed-red line shows the reference beam path.

optical-turbulence scenarios. In this setup, phase screens were imposed on the beam using SLMs. This allows you to include many of the effects that exist in real systems such as imperfect laser sources, optical alignment, camera noise, etc. The system used in this experiment is shown in Fig. 2. Here, a 633 nm laser source with a coherence length of approximately 100 m was expanded to a 5.4 mm Gaussian beam. This beam was reflected off of the first SLM at an angle. A diffraction pattern is created when the beam reflects off of the SLM due to a slight gap between the SLM's liquid-crystal pixels. To address this, we added a tilt angle of 2.35×10^{-2} radians to the SLM in addition to turbulent phase screen. After reflecting off the SLM, this additive tilt allowed us to separate the desired signal from the diffractive signal using an iris. After the SLM, the beam passes through the optical trombone which consists of two turning flats mounted on a linear traverse. The beam then passes through a 4f reimaging system to relay the beam to the next SLM. The beam again passes through the optical trombone and then through another 4f reimaging system. At the exit of the turbulence-generator system, the beam was apertured using an iris. Subsequently, the beam was relayed to a suite of sensors including a SHWFS, DHWFS, and an imaging camera.

When the optical trombones are in their home position, both SLMs, the exit pupil of the system, as well as the wavefront sensor suite are conjugate to each other. By moving the optical trombones, we can replicate a given propagation distance. For some of the tests described in the next section, we selected the optical-trombone position such that the replicated propagation distance matched the propagation distance defined in the wave-optics simulations.

4. SYSTEM CHARACTERIZATION

To characterize our system, we first imposed single phase screens of varying turbulence strengths onto the SLMs, one SLM at a time. Initially, we set the optical trombones in their home position such that only phase aberrations were imposed onto the beam. Next, we moved the optical trombones from their home position to introduce scintillation in addition to phase aberrations. For both of these tests, complementary wave-optics

simulations were also conducted using the same phase screens applied to the SLMs. In what follows, we discuss the details of these tests and describe the results in earnest.

4.1 Varying turbulence strength

To test the turbulence strength scaling, we applied 10 phase screens to a single SLM with increasing C_n^2 values from $7{\times}10^{-15}$ to $3.5{\times}10^{-14}$ $m^{-2/3}$. $Z = 1000$ m was used for the generation of all the phase screens. The random number generator seed used to create the phase screens was set to be constant for each screen so that only the amplitude of the phase fluctuations was changing. For this test, both optical trombones were set at their home position. Therefore, as described above, the SLMs were conjugate to the entrance pupils of both wavefront sensors; thereby eliminating any scintillation caused by propagation.

The measured wavefronts were compared to the simulation results, first by comparing with the digital holography measurements. To carry out these tests, we needed to ensure that the experimental setup was spatially aligned to the simulation grid. To accomplish this, we first imposed a phase field in the shape of a pyramid on the SLM centered at the origin. This provided a clear object showing axis directions and scaling in x, y, and z. The higher resolution simulation wavefront was downscaled using cubic interpolation so that the pixel width was the same as the digital holography wavefront, then the pixels were shifted to align them. Alignment was only up to the closest pixel shift and rotation was not accounted for. A common mask was then applied to both images and tip/tilt was removed from both. The aligned location was saved and this alignment procedure was then used for all subsequent tests.

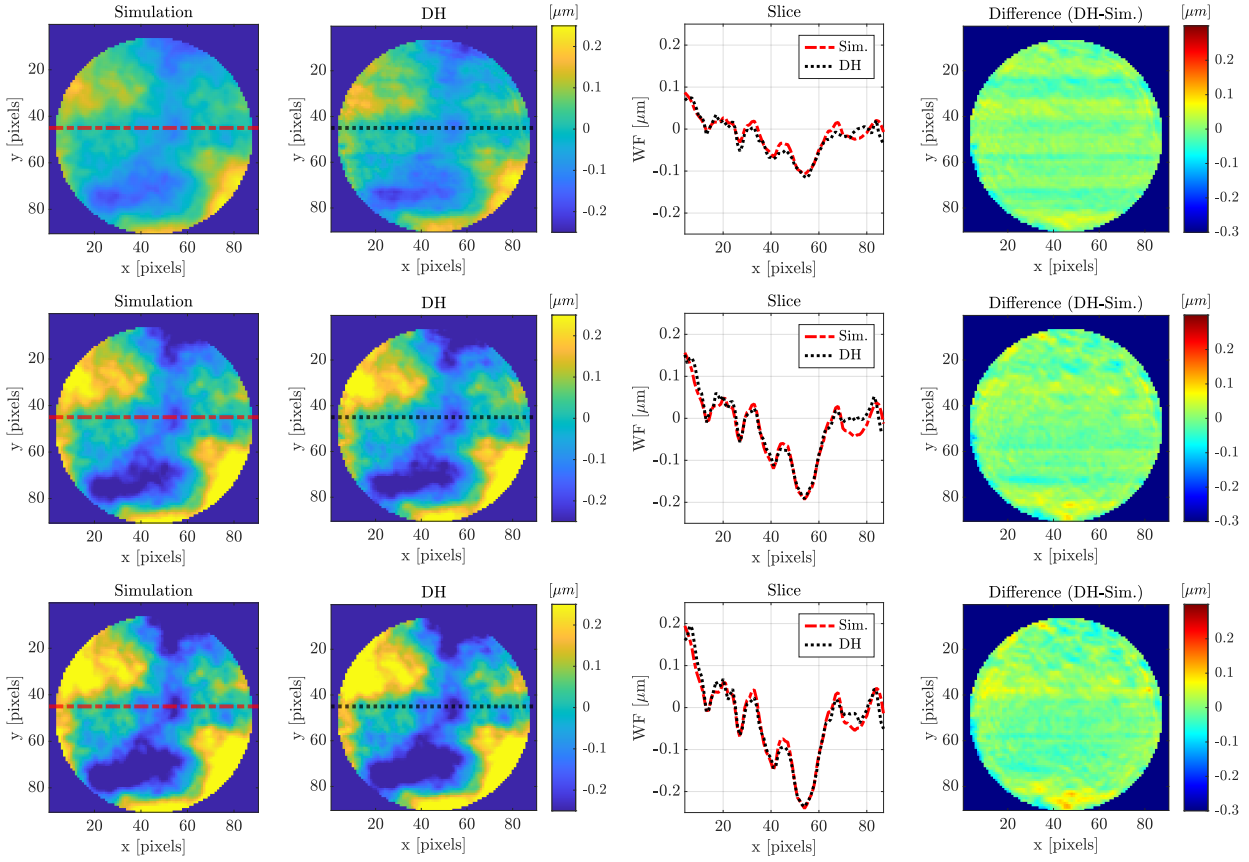


Figure 3. First column shows WF computed in simulation, second column is WF measured by digital holography, third column is a slice through both wavefront, and the fourth column is the difference between the DH and Simulation wavefronts. Rows 1-3 are for $C_n^2 = 7 \times 10^{-15}$, 2.1×10^{-14}, 3.5×10^{-14} $m^{-2/3}$ respectively.

The resulting simulation and DH wavefronts are shown in Fig. 3 in the first and second columns, respectively. Rows 1–3 are for $C_n^2 = 7{\times}10^{-15}$, $2.1{\times}10^{-14}$, and $3.5{\times}10^{-14}$ $m^{-2/3}$. For all three cases, the simulated and experimentally measured wavefronts appear nearly identical. The third column of Fig. 3 compares a one-dimensional slice of the simulation and DH wavefronts. Here, it is clear that the simulation and experimental results are in close agreement. The last column of the figure shows a spatial map of the difference in measured phase between the simulated and experimentally measured wavefronts for each case. Here, we see that there is fairly consistent error across all cases. By taking the spatial standard deviation of the difference in measured phase, we get the root mean square error (RMSE) for each case. Here we calculated the RMSE to be approximately 0.021 μm, 0.024 μm, and 0.029 μm for the weak, medium, and strong cases, respectively. Some horizontal striations are visible in the DH wavefronts and the difference maps, and are most clear in the weakest turbulence case. These are from diffraction off the SLM which was explained in Sec. 2.2. In the Fourier plane, these lines manifest as horizontally distributed peaks which are visible on some of the peaks in top right image of Fig. 1, such as the one at (200,200). An attempt was made to filter out most of the diffraction peaks in the Fourier plane using a carefully selected circular mask size which helped reduce the horizontal striations and slightly improved the RMSE of the DH wavefront. However, the stronger turbulence cases have a larger farfield pattern in the Fourier plane which leads to greater overlap with some of the spurious diffraction peaks. Therefore, masking out the diffraction peaks resulted in also masking out some of the desired signal, leading to worse performance. Thus, this filtering was not used. Overall, the analysis presented here shows that we are able to generate a phase screen in simulation, apply it in our turbulence generator, and then accurately measure the applied phase aberration with our wavefront sensor. Furthermore, we showed the simulation and DHWFS results to be in close agreement. We conducted the same procedure by applying phase screens to the second SLM and achieved similar results.

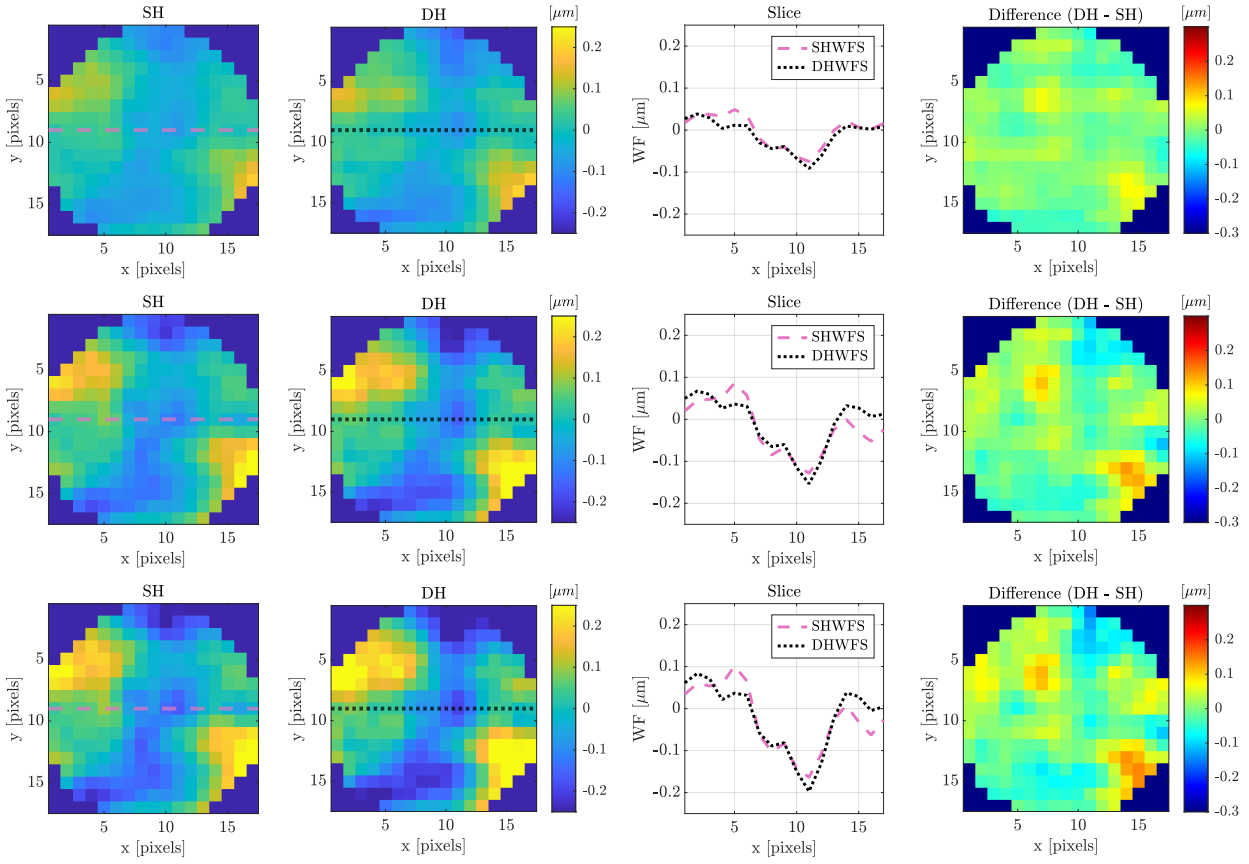


Figure 4. First column shows WF measured by the SHWFS, second column is WF measured by the DHWFS, third column is a slice through both wavefront, and the fourth column is the difference between the DH and SH wavefronts.

Next, we compared the DHWFS and SHWFS results by aligning and downsampling the DH wavefront (same as was done when we compared the simulated wavefront and DHWFS results). The SH and DH wavefronts are shown in the first and second columns of Fig. 4, again with a slice shown in the third column and the difference maps in the last column. The same three turbulence cases are shown as in Fig. 3. We first can see how the SHWFS results in a much lower resolution WF. The SH and DH wavefronts appear similar. From the slice and difference maps, the SH and DH do not agree as well as DH agreed with simulation. The root mean square difference is 0.026 μm, 0.043 μm, and 0.053 μm for the weak, medium, and strong turbulence cases. However, it is interesting that the difference seems to scale with turbulence as well. For example, the SH wavefront has a lower value at (15,15), and the relative difference between the SH and DH wavefronts at that location gets larger for stronger turbulence case. This suggests that it is not a result of non-common path aberrations between the two sensors, misalignment of the images, or random noise. However, there are many other potential sources for this difference including non-uniform illumination corrupting the SHWFS tilt measurements, fitting error from SH reconstruction, or from downscaling the DH wavefront.

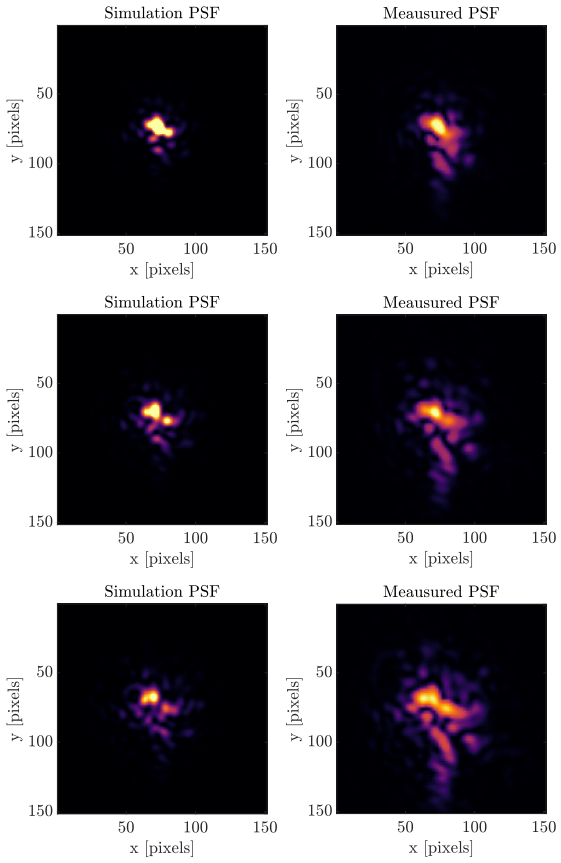


Figure 5. First column shows farfield irradiance from simulation, second column is the farfield irradiance measured on the camera.

The point spread function (PSF) of the beam in the image plane was also measured and compared to simulation. The point spread function of the simulation was created by propagating the 0.25 m beam through a lens with a focal length 1.31 km such that the number of pixels across the farfield irradiance pattern was the same as the camera measurement. The simulation and measured PSFs are shown in Fig. 5 on the left and right. The rows correspond to the same turbulence strengths as the previous figures. The irradiance of these images was normalized by the maximum irradiance of a PSF that was not subjected to turbulence. Specifically, we normalized the simulated PSF by the maximum irradiance of a diffraction-limited PSF and we normalized the experimentally measured PSF by the maximum irradiance from the baseline measurement. From these results,

we see that the simulation PSF looks similar to the measured PSF, however, the measured PSF has more beam spread. For both, we see beam spread increase with increasing turbulence strength.

4.2 Varying propagation

The next analysis tested the propagation scaling of the system and looked at scintillation effects. In this case, we applied the strongest phase screen tested in the last analysis where $C_n^2 = 3.5 \times 10^{-14}\ m^{-2/3}$, then moved the optical trombone to add propagation distances of 0–46.6 cm. The same scenarios were performed in simulation. Scaling between simulation and our benchtop testing was accomplished by matching the Fresnel number, $F = \frac{Z^2}{\lambda D}$ where Z is the propagation distance and D is the beam width. In simulation, we defined $D = 0.25$ m. Therefore, the 0–46.6 cm additive propagation distance on the optical trombone corresponded to propagation distances between 0–1 km in simulation.

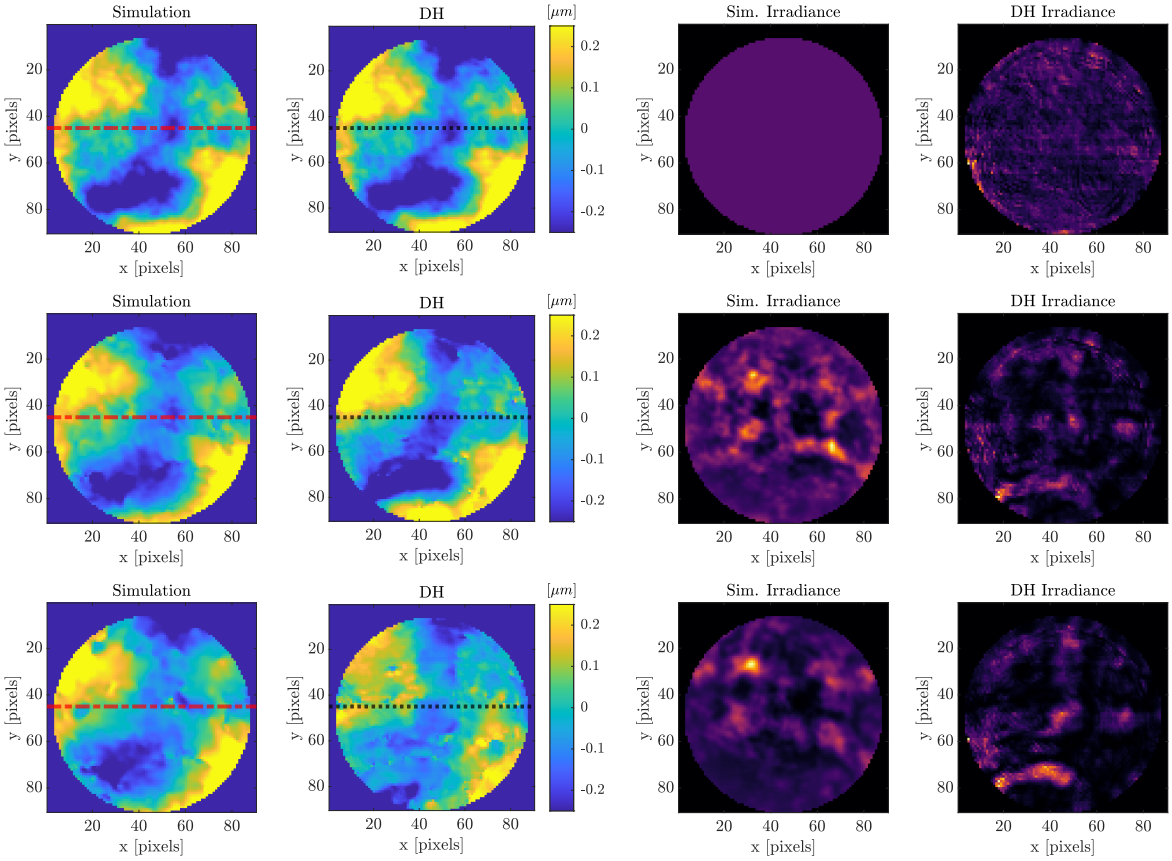


Figure 6. First column shows WF measured by simulation, second column is WF measured by digital holography, third column is the pupil irradiance calculated in simulation, and the fourth column is the pupil irradiance measured by digital holography.

The same WF alignment and rescaling procedure was used as before to compare the simulated phase with the measured DH wavefronts which are shown in the first and second columns of Fig. 6. Each row has increasing propagation length with the first row showing $Z = 0$, followed by $Z = 0.5$ km and $Z = 1$ km in the next two rows. The $Z = 0$ wavefronts are the same as before and are very similar. However, as we increase propagation distance, the agreement begins to diminish. For the $Z = 1$ km case, the phase has the same low frequency content, but the higher frequency structures no longer look similar. The RMSE for the $Z = 0$, $Z = 0.5$, and $Z = 1$ km cases were 0.029 μm, 0.085 μm, and 0.103 μm, respectively.

The pupil irradiance was also compared to look at how well the system captures scintillation. The simulation irradiance pattern was rescaled and aligned with the DH measured pupil irradiance following the same procedure

used to align wavefronts in Sec. 4.1. The initial Gaussian irradiance profile was removed from the simulation irradiance to match the processing used for the experimental digital holography data, so the simulation irradiance is one for the $Z = 0$ case. The pupil irradiance fluctuation maps for the simulated and DH results are shown in the third and fourth columns of Fig. 6, respectively. Here we see that the DH measured irradiance resembles the simulated results, however, there are noticeable variations. As expected, there is minimal scintillation measured for the $Z = 0$ km case. For the $Z = 0.5$ km and $Z = 1$ km cases, we see that the peaks and valleys of both the simulated and measured irradiance patterns look similar; however, it seems like the DH irradiance patterns are shifted downward relative to the simulated irradiance patterns. Furthermore, we again see faint horizontal striations in the DH results due to the diffraction of the beam from the SLM. There are also some concentric patterns near the edges of the beam. We speculate that these artifacts are from the iris that was used to aperture the beam just before it entered the sensing suite. This iris was not at a conjugate plane leading to the onset of additional diffractive effects.

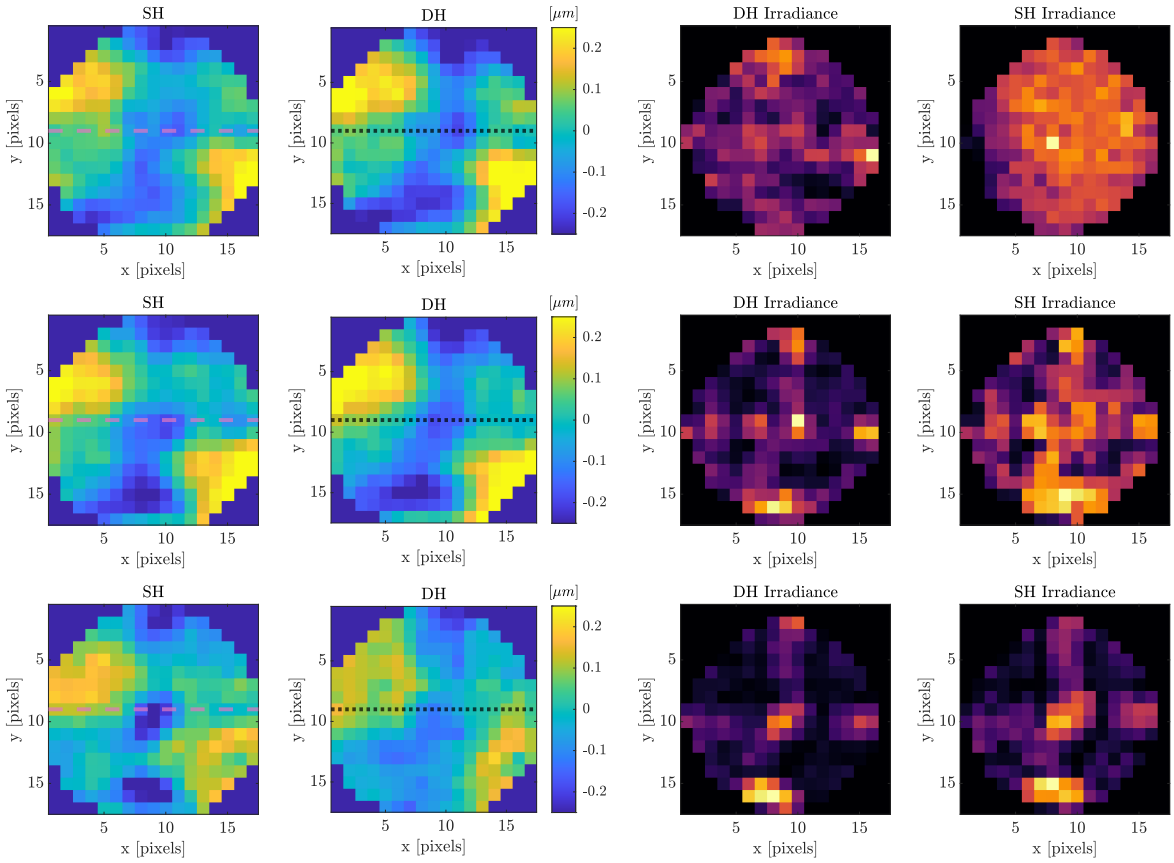


Figure 7. First column shows WF measured by the SHWFS, second column is WF measured by the DHWFS, third column the pupil irradiance measured by the DHWFS, and the fourth column is the pupil irradiance measured by the SHWFS.

The SHWFS wavefront was then compared with DHWFS wavefront as before, and the $Z = 0, 0.5, 1$ km cases are shown in Fig. 7. The $Z = 0$ case in the top row is the same as the highest turbulence case discussed before and agrees well. The $Z = 0.5$ km case also agrees well with SH having a larger value in the region around (10,6). For the last case at $Z = 1$ km, we see similar large scale structures, but the smaller structures are different, with the SH wavefront having higher peaks and lower valleys. The RMSE for the $Z = 0$, $Z = 0.5$, and $Z = 1$ km cases were 0.053 μm, 0.049 μm, and 0.068 μm, respectively.

The irradiances were also compared. The irradiance of the SHWFS was taken to be the total irradiance of a given area of interest (AOI) in the SHWFS image. Note that the baseline irradiance was not removed from the

SH irradiance, so for the $Z = 0$, the DH irradiance shown in the third column of Fig. 7 is much flatter than the SH irradiance which is in the fourth column. The $Z = 0.5$ km looks similar between the two, while the $Z = 1$ km case looks very similar.

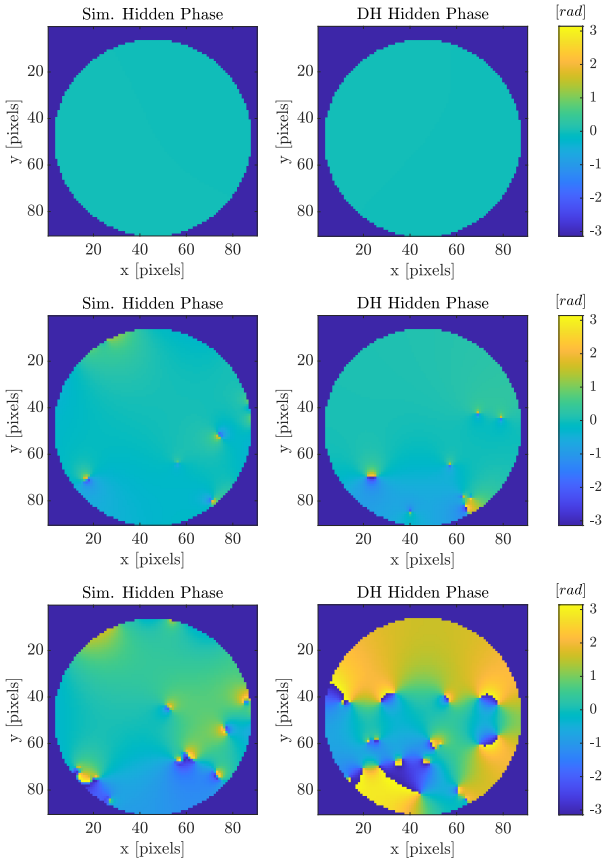


Figure 8. First column shows simulated hidden phase. The second column shows the DH hidden phase.

Adding propagation effects also allows for us to explore the number and locations of branch points within the pupil. As described in the introduction, when SHWFS data are used in a least-squares reconstruction algorithm, the resultant wavefront estimate does not contain branch points. However, we were able to identify branch points from both the simulated as well as DHWFS data. The hidden phase for both the simulation and DH complex-optical fields was found by subtracting the unwrapped phase from the wrapped phase. The simulation and DH hidden phase are shown in the first and second columns of Fig. 8, where each row corresponds to the increasing propagation distances. For both the simulation and DH hidden-phase fields, we see that there are no branch points present for the $Z = 0$ km case. This is expected since the beam has not propagated and therefore, there is no diffraction. For the $Z = 0.5$ km case, we now see that some branch points are present across the pupil. The hidden phase looks similar between the simulation and DH results, with branch point pairs appearing in similar locations. The DH hidden phase has a few more branch points and this is likely due to noise in the phase measurement, which can also lead to branch points noise in the phase measurement, which can also lead to branch points. The windowed average filter was found to help reduce noise and consequently, the number of noise-related branch points. For the longest propagation case of $Z = 1$ km, the DH hidden phase does not appear very similar to the simulation hidden phase and has more branch points.

Before moving on, it is also worth pointing out the difference in branch-cut length between the $Z = 0.5$ km and $Z = 1$ km cases. It has been shown that after branch-point pairs form, branch-points persist upon further propagation; however, they begin to spatially separate.[32–34] The spatial separation of branch-point pairs with propagation distance results in longer branch cuts; which we see here.

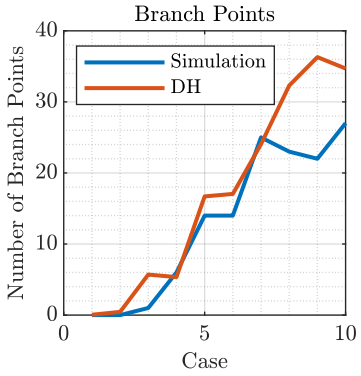


Figure 9. Number of branch points for cases of increasing propagation length.

The number of branch points was calculated for each propagation distance case using the phase gradient approach [1,12] and are plotted in Fig. 9. While the DH phase contains more branch points due to measurement noise, the number of branch points trends similarly.

4.3 Turbulence statistics

The previous two analyses gave a primarily qualitative look at how the turbulence-generator system compares to the wave-optics simulation we wish to replicate. In this section, we quantitatively look at how well the system is able to replicate phase and amplitude effects of propagation through turbulence. Wave-optics simulations were run for a 0.25 m collimated beam propagating 1 km, with two phase screens equally spaced along the path. Ten C_n^2 values were used to create the phase screens varying from $C_n^2 = 9.9 \times 10^{-16}$ to 9.9×10^{-15} $m^{-2/3}$ with corresponding Rytov numbers of 0.01–0.14. One hundred random phase screens were created and tested for each C_n^2 in a Monte–Carlo fashion.

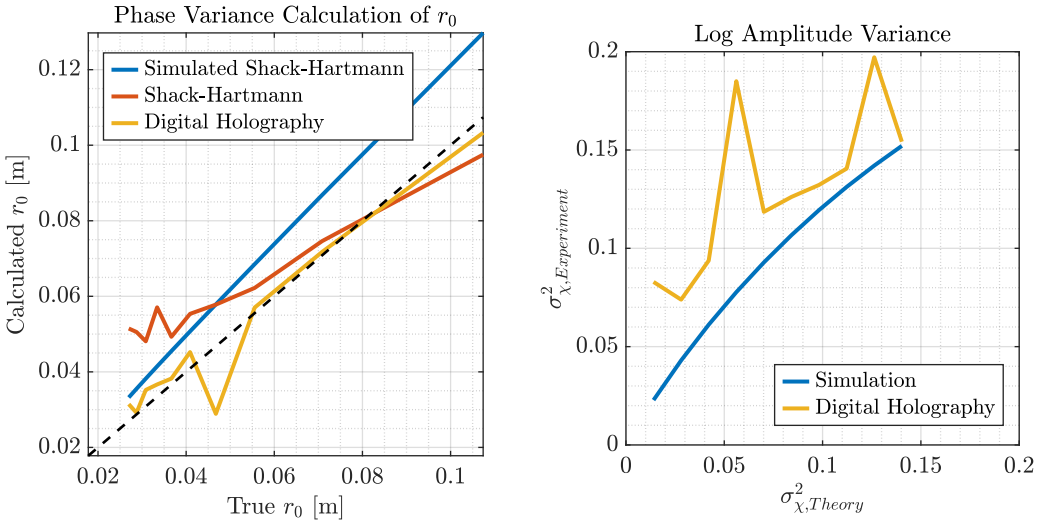


Figure 10. r_0 calculated from different wavefront measurements, plotted against the r_0 calculated from the C_n^2 used to define the phase screens(left). Log-amplitude variance from pupil irradiance plotted as a function of log-amplitude variance expected based on C_n^2 of phase screens.

The first metric of interest was the Fried parameter, r_0, which can be related to C_n^2 as

$$r_0 = 1.68(k^2 Z C_n^2)^{-3/5} \tag{1}$$

for C_n^2 that is constant along the propagation path, where $k = \frac{2\pi}{\lambda}$. This was calculated from the measured phase using the tilt-removed phase variance, σ_ϕ^2

$$\sigma_\phi^2 = 0.134 \left(\frac{D}{r_0}\right)^{5/3}, \tag{2}$$

where D is the aperture diameter.[35] As discussed in the introduction, the slope estimates obtained with the SHWFS are traditionally used in a least-squares reconstructor to estimate the continuous $OPD(x, y, t)$. After removing tip, tilt, piston, and lensing aberrations from the reconstructed $OPD(x, y, t)$ field, the OPD_{RMS} was calculated by taking the root-mean-square over the spatial dimension and temporally averaging for each data point. Subsequently, the OPD_{RMS} calculated for each data collection was used to calculate the least-squares phase variance as, $\sigma_{\phi,LS}^2 = \left[-2\pi OPD_{RMS}/\lambda\right]^2$. Here, we assume that the $\sigma_{\phi,LS}^2 \approx \sigma_\phi^2$. Under this assumption, we can use the $\sigma_{\phi,LS}^2$ calculated from the reconstructed SHWFS measurements to solve for r_0 in Eq. 2. The calculated Monte–Carlo averaged r_0 values are shown in left plot of Fig. 10. Here the blue line shows the r_0 calculated from a simulated SHWFS used in the simulation. This value overestimates the true r_0. The red line represents the r_0 calculated from the SHWFS measurement. This also overestimates r_0 for the strong turbulence strengths, but then underestimates for the large r_0 cases. For the large r_0 cases, the turbulence is weak, so it is possible that non-uniform illumination due to diffraction from the SLM is causing more phase fluctuations and increasing the phase variance. The r_0 from the digital holography measurement is very close to the true r_0, except for one value which underestimated r_0 for the true r_0 of 0.045 m.

To quantify scintillation, the measured amplitude variance was compared to the Rytov number (log-amplitude variance) where the Rytov number is related to a constant C_n^2 by

$$\sigma_{\chi,Theory}^2 = 0.307 k^{7/6} Z^{11/6} C_n^2 \tag{3}$$

for a collimated beam. The log-amplitude variance was calculated from the measured pupil irradiance as[36]

$$\sigma_{\chi,Experiment}^2 = \frac{1}{4} \ln\left(\frac{\langle I^2(r)\rangle}{\langle I(r)\rangle^2} + 1\right) \tag{4}$$

where r is the radial distance from the beam center and the angle brackets denote ensemble averaging, which in this case was an average across the Monte–Carlo iterations. The resulting log-amplitude variances were spatially averaged and plotted against the Rytov number defined by the simulation C_n^2 values in the right plot of Fig. 10. The log-amplitude variance of the simulation pupil irradiance is shown by the blue line. This trends just about a one-to-one relation with the Rytov number. The log-amplitude variance of the DH measured irradiance is close to the log-amplitude variance from simulation, with some overestimation for lower log-amplitude cases. This overestimation is likely from the diffraction pattern that was seen in Section 4.2.

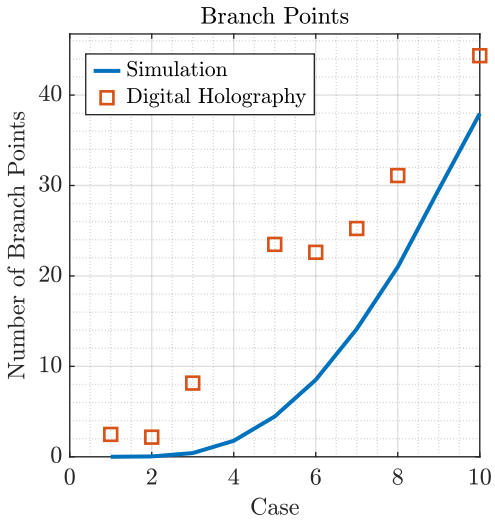


Figure 11. Number of branch points calculated for each case.

The number of branch points was calculated again to see how well the hidden phase was being captured and is plotted for each turbulence strength. The number of branch points from the simulation is shown by the blue line in Fig. 11, while the number from the DH measurement is shown by orange squares. The number of branch points in the DH follows a similar trend to the simulation, except they are offset by about 2-10 branch points. Cases 4 and 9 have a significantly larger number of branch points and are the same cases that have much larger amplitude variance in Fig. 10. The increased number of branch points found in the DH data is likely from noise.

5. CONCLUSION

In this work, SHWFS, off-axis DH, and farfield image measurements were taken to characterize a benchtop optical turbulence simulator system. This system used two SLMs to impose turbulence phase screens with prescribed turbulence statistics onto the beam. Three sets of tests were run and compared to wave-optics simulations to characterize different components of the system. The first varied the turbulence strength on a single SLM with the optical trombones set at their home position. This allowed us to investigate the system's ability to impose phase disturbances. The SH and DH measured wavefronts were compared directly to the wavefront found in simulation, in this case just the phase screen converted to an unwrapped wavefront. The DH wavefronts had a RMSE of 0.02 μm - 0.03 μm compared to the simulated wavefront, while the SH wavefront had an RMSE of 0.02 μm - 0.05 μm compared to the DH wavefront. There were some diffraction effects from the SLMs that contaminated the measured wavefront and irradiance. The farfield irradiance was also measured and compared with simulation. Similar shapes were found, however, the measured irradiance had more significant beam spread.

The second test used one phase screen but moved the optical trombone away from its home position. This allowed us to explore the system's ability to model beam propagation. Here the wavefront and pupil irradiance were compared between the sensors and simulation. For longer propagation distances, the phase disagreement increased with RMSE between the simulation and DH going from 0.029 μm for $Z = 0$ to 0.10 μm for $Z = 1$ km. The disagreement between SH and DH also increased with propagation, although less dramatically, going from 0.05 μm to 0.07 μm. The pupil irradiance was found to have similar trends and arguably similar shapes, but the agreement was much worse than the wavefront. The hidden phase from simulation and from the DH measurement were also compared and found to be similar up to 0.5 km propagation with similar branch point locations. For the longer propagation of 1 km, the number of hidden phase were fairly different between simulation and DH. However, the number of branch points was found to agree well over the whole range of propagation distances.

The final test used both SLMs to model propagation of a 25 cm beam along a 1 km path in a Monte–Carlo fashion using 100 independent sets of phase screens, allowing us to characterize the system's ability to model turbulence parameters. The Fried parameter, r_0, was calculated from the phase variance for each sensor and

compared to the true r_0 calculated from the C_n^2 defining the phase screens. The DH measurement agreed very well with the true r_0, while the SH measurements were similar but underestimated turbulence strength for small r_0. A simulated SHWFS was applied in simulation and this was found to underestimate turbulence strength over the entire range of conditions tested. Log-amplitude variance, σ_χ^2 was compared to the Rytov number finding the σ_χ^2 from simulation and DH to be slightly larger than the Rytov number, while the SH amplitude variance was larger and had more variation. The number of branch points in the hidden phase were also calculated and DH was found to follow a similar trend as simulation, but with more branch points likely due to noise in the phase.

In summary we have setup and characterized a SLM-based benchtop optical-turbulence simulator. This testbed will allow us to conduct beam propagation, imaging, and adaptive-optics experiments.

ACKNOWLEDGMENTS

Grateful acknowledgement is given to ONR whose sponsorship and continuing guidance of the IAR program has made this research possible. These efforts were funded under ONR award N0001423WX00073.

Distribution Statement A. Approved for public release: distribution is unlimited. Public Affairs release approval #: NSWCDD-PN-24-00216

6. DISCLOSURES

The U.S. Government is authorized to reproduce and distribute reprints for governmental purposes notwithstanding any copyright notation thereon.

REFERENCES

[1] Fried, D. L. and Vaughn, J. L., "Branch cuts in the phase function," *Appl. Opt.* **31**, 2865–2882 (May 1992).

[2] Barchers, J. D., Fried, D. L., and Link, D. J., "Evaluation of the performance of hartmann sensors in strong scintillation," *Applied Optics* **41**, 1012 (feb 2002).

[3] Holmes, R. B., "Scintillation-induced jitter of projected light with centroid trackers," *J. Opt. Soc. Am. A* **26**, 313–316 (Feb 2009).

[4] Fried, D. L., "Branch point problem in adaptive optics," *J. Opt. Soc. Am. A* **15**, 2759–2768 (Oct 1998).

[5] Tyler, G. A., "Reconstruction and assessment of the least-squares and slope discrepancy components of the phase," *Journal of the Optical Society of America* **17**, 1828 (oct 2000).

[6] Wild, W. J. and Bigot, E. O. L., "Rapid and robust detection of branch points from wave-front gradients," *Optics Letters* **24**, 190 (feb 1999).

[7] Chen, M., Roux, F. S., and Olivier, J. C., "Detection of phase singularities with a shack-hartmann wavefront sensor," *Journal of the Optical Society of America A* **24**, 1994 (jun 2007).

[8] Chen, M. and Roux, F. S., "Dipole influence on shack-hartmann vortex detection in scintillated beams," *Journal of the Optical Society of America A* **25**, 1084 (apr 2008).

[9] Murphy, K., Mackey, R., and Dainty, C., "Branch point detection and correction using the branch point potential method," in [*SPIE Proceedings*], Gilbreath, G. C. and Wasiczko, L. M., eds., SPIE (apr 2008).

[10] Kalensky, M., "Branch-point identification using second-moment shack hartmann wavefront sensor statistics," *Applied Optics* **62**, G101 (may 2023).

[11] Kalensky, M., Oesch, D., Bukowski, T. J., Miller, K., and Getts, D., "Branch-point detection using a shack-hartmann wavefront sensor," in [*Unconventional Imaging, Sensing, and Adaptive Optics 2023*], Bose-Pillai, S. R., Dolne, J. J., and Spencer, M. F., eds., SPIE (oct 2023).

[12] Kalensky, M., Oesch, D. W., Bukowski, T. J., Miller, K., and Getts, D., "Comparison of branch-point detection approaches using a shack hartmann wavefront sensor," *Optical Engineering* **62** (Dec. 2023).

[13] Steinbock, M. J., *Implementation of Branch-Point-Tolerant Wavefront Reconstructor for Strong Turbulence Compensation*, master's thesis, Air Force Institute of Technology, Wright-Patterson Air Force Base, OH (June 2012). https://apps.dtic.mil/sti/citations/ADA562776.

[14] Spencer, M. F., Raynor, R. A., Banet, M. T., and Marker, D. K., "Deep-turbulence wavefront sensing using digital-holographic detection in the off-axis image plane recording geometry," *Optical Engineering* **56**(3), 031213 (2016).

[15] Banet, M. T., Spencer, M. F., and Raynor, R. A., "Digital-holographic detection in the off-axis pupil plane recording geometry for deep-turbulence wavefront sensing," *Appl. Opt.* **57**, 465–475 (Jan 2018).

[16] Thornton, D. E., Spencer, M. F., and Perram, G. P., "Deep-turbulence wavefront sensing using digital holography in the on-axis phase shifting recording geometry with comparisons to the self-referencing interferometer," *Appl. Opt.* **58**, A179–A189 (Feb 2019).

[17] Spencer, M. F., "Spatial heterodyne," in [*Encyclopedia of Modern Optics (Second Edition)*], Guenther, B. D. and Steel, D. G., eds., 369–400, Elsevier, Oxford, second edition ed. (2018).

[18] Horst, S., Radosevich, C. J., Pellizzari, C. J., and Spencer, M. F., "Measuring the Fried parameter of transmissive phase screens using digital-holographic detection," in [*Unconventional and Indirect Imaging, Image Reconstruction, and Wavefront Sensing 2019*], Dolne, J. J., Spencer, M. F., and Testorf, M. E., eds., **11135**, 111350D, International Society for Optics and Photonics, SPIE (2019).

[19] Horst, S. B., Oesch, D. W., and Sexauer, M. S., "Measurement of turbulence parameters induced by the reflective atmospheric turbulence simulator," in [*Unconventional Imaging, Sensing, and Adaptive Optics 2023*], Dolne, J. J., Spencer, M. F., and Bose-Pillai, S. R., eds., **12693**, 126931L, International Society for Optics and Photonics, SPIE (2023).

[20] Rasouli, S., Razi, E. M., and Niemela, J. J., "Investigation of the anisotropy and scaling of the phase structure function of a spatially coherent light beam propagating through convective air turbulence," *J. Opt. Soc. Am. A* **39**, 1641–1649 (Sep 2022).

[21] Dayton, D. C. and Spencer, M. F., "Scaled-laboratory demonstrations of deep-turbulence conditions," *Appl. Opt.* **63**, E54–E63 (Jun 2024).

[22] Kalensky, M., Spencer, M. F., Jumper, E. J., and Gordeyev, S., "Estimation of atmospheric optical turbulence strength in realistic airborne environments," *Applied Optics* **61**, 6268 (jul 2022).

[23] Bukowski, T. J., O'Sullivan, S., Kalensky, M., Getts, D., Bates, E. M., Miller, K., and Gordeyev, S., "Optical-turbulence characterization of a littoral test environment using a Shack-Hartmann wavefront sensor," in [*Unconventional Imaging, Sensing, and Adaptive Optics 2023*], Dolne, J. J., Spencer, M. F., and Bose-Pillai, S. R., eds., **12693**, 126930Q, International Society for Optics and Photonics, SPIE (2023).

[24] Wilcox, C. C., Radosevich, C. J., Healy, K. P., Tuffli, A. L., Agena, B. D., and Mark F. Spencer, D. J. W. I., "Digital holography wavefront sensing with a super wind tunnel," **11030**, SPIE (April 2019).

[25] Chu, E. D., Bukowski, T. J., and Gordeyev, S., "Studies of local shock effects on Shack-Hartmann and digital holography wavefront sensors," in [*Unconventional Imaging, Sensing, and Adaptive Optics 2023*], Dolne, J. J., Spencer, M. F., and Bose-Pillai, S. R., eds., **12693**, 1269317, International Society for Optics and Photonics, SPIE (2023).

[26] Schmidt, J., [*Numerical simulation of optical wave propagation with examples in MATLAB*], SPIE, Bellingham, Wash (2010).

[27] Martin, J. M. and Flatté, S. M., "Intensity images and statistics from numerical simulation of wave propagation in 3-d random media," *Applied Optics* **27**, 2111 (jun 1988).

[28] Martin, J. M. and Flatté, S. M., "Simulation of point-source scintillation through three-dimensional random media," *Journal of the Optical Society of America* **7**, 838 (may 1990).

[29] Knepp, D., "Multiple phase-screen calculation of the temporal behavior of stochastic waves," *IEEE* **71**(6), 722–737 (1983).

[30] MACASKILL, C. and EWART, T. E., "Computer simulation of two-dimensional random wave propagation," *IMA Journal of Applied Mathematics* **33**(1), 1–15 (1984).

[31] Roggemann, M., [*Imaging through turbulence*], CRC Press, Boca Raton (1996).

[32] Oesch, D. W., Sanchez, D. J., and Matson, C. L., "The aggregate behavior of branch points - measuring the number and velocity of atmospheric turbulence layers," *Optics Express* **18**, 22377 (oct 2010).

[33] Oesch, D. W., Sanchez, D. J., and Tewksbury-Christle, C. M., "Aggregate behavior of branch points - persistent pairs," *Optics Express* **20**, 1046 (jan 2012).

[34] Oesch, D. W., Tewksbury-Christle, C. M., Sanchez, D. J., and Kelly, P. R., "Aggregate behavior of branch points: characterization in wave optical simulation," *Optical Engineering* **51**, 106001 (oct 2012).
[35] Noll, R. J., "Zernike polynomials and atmospheric turbulence∗," *J. Opt. Soc. Am.* **66**, 207–211 (Mar 1976).
[36] Fried, D. L., "Aperture averaging of scintillation," *J. Opt. Soc. Am.* **57**, 169–175 (Feb 1967).